THE JOURNAL OF PHYSICAL CHEMISTRY C

Article

Cite This: J. Phys. Chem. C 2019, 123, 10346−10355

pubs.acs.org/JPCC

Effect of HF Pressure on Thermal Al_2O_3 Atomic Layer Etch Rates and Al_2O_3 Fluorination

Published as part of The Journal of Physical Chemistry virtual special issue "Hanna Reisler Festschrift".

Austin M. Cano, Amy E. Marquardt, Jaime W. DuMont, and Steven M. George*

Department of Chemistry, University of Colorado, Boulder, Colorado 80309-0215, United States

ABSTRACT: Thermal Al_2O_3 atomic layer etching (ALE) can be accomplished using sequential fluorination and ligand-exchange reactions. HF can be employed as the fluorination reactant, and $Al(CH_3)_3$ can be utilized as the metal precursor for ligand exchange. This study explored the effect of HF pressure on the Al_2O_3 etch rates and Al_2O_3 fluorination. Different HF pressures ranging from 0.07 to 9.0 Torr were employed for Al_2O_3 fluorination. Using *ex situ* spectroscopic ellipsometry (SE) measurements, the Al_2O_3 etch rates increased with HF pressures and then leveled out at the highest HF pressures. Al_2O_3 etch rates of 0.6, 1.6, 2.0, 2.4, and 2.5 Å/cycle were obtained at 300 °C for HF pressures of 0.17, 0.5, 1.0, 5.0, and 8.0 Torr, respectively. The thicknesses of the corresponding fluoride layers were also measured using X-ray photoelectron spectroscopy (XPS). Assuming an Al_2OF_4 layer on the Al_2O_3 surface, the fluoride thicknesses increased with HF pressures and reached saturation values at the highest HF pressures. Fluoride thicknesses of 2.0, 3.5, 5.2, and 5.5 Å were obtained for HF pressures of 0.15, 1.0, 4.0, and 8.0 Torr, respectively. There was an excellent correlation between the Al_2O_3 etch rates and fluoride layer thicknesses versus HF pressure. In addition, *in situ* Fourier transform infrared spectroscopy (FTIR) vibrational studies were used to characterize the time dependence and magnitude of the Al_2O_3 fluorination. These FTIR studies observed the fluorination of Al_2O_3 to AlF_3 or AlO_xF_y by monitoring the infrared absorbance from the Al−O and Al−F stretching vibrations. The time dependence of the Al_2O_3 fluorination was explained in terms of rapid fluorination of the Al_2O_3 surface for initial HF exposures and slower fluorination into the Al_2O_3 near surface region that levels off at longer HF exposure times. Fluorination into the Al_2O_3 near surface region was described by parabolic law behavior. The self-limiting fluorination of Al_2O_3 suggests that the fluoride layer on the Al_2O_3 surface acts as a diffusion barrier to slow the fluorination of the underlying Al_2O_3 bulk. For equal fluorination times, higher HF pressures achieve larger fluoride thicknesses.

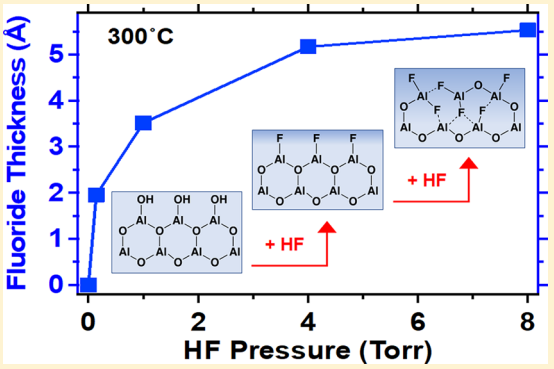

I. INTRODUCTION

Atomic layer etching (ALE) is based on sequential, self-limiting surface reactions that can remove material from surfaces with atomic layer control.[1] Some ALE methods are based on plasma techniques that utilize sequential surface modification and removal reactions.[1] The surface modification can involve surface chlorination or oxidation. The removal is accomplished with ions or energetic neutral atoms to obtain etching. These plasma ALE processes can achieve anisotropic etching. Examples of plasma ALE include Si,[2−4] Ge,[5] GaAs,[6] SiO_2,[7,8] HfO_2,[9] Si_3N_4,[10] graphite,[11] and polymer[12] ALE.

Other ALE methods are based on thermal chemistry.[13] These thermal ALE processes are also performed using surface modification and removal reactions. The surface modification can be accomplished by surface fluorination or oxidation. For thermal ALE, the removal reaction is a thermal reaction such as ligand-exchange[13,14] or fluorination to a volatile fluoride.[15] These thermal ALE processes can achieve isotropic etching. Examples of thermal ALE include Al_2O_3,[13,16−19] HfO_2,[20,21] SiO_2,[22] ZnO,[23] TiO_2,[24] WO_3,[25] W,[25,26] TiN,[15] and AlN[27] ALE.

Many thermal ALE processes are based on sequential fluorination and ligand-exchange reactions.[13,14] In this etching process for a metal oxide, the surface of the metal oxide is first fluorinated to form a thin metal fluoride layer on the metal oxide.[13,18] Subsequently, the thin metal fluoride layer is removed with a ligand-exchange reaction.[13,18] During this ligand-exchange reaction, a metal precursor accepts fluorine from the metal fluoride and concurrently transfers one of its ligands to the metal fluoride. The ligand-exchange reaction can produce reaction products from the metal fluoride that desorb into the gas phase. The sequential application of fluorination and ligand-exchange reactions progressively removes the metal oxide. This thermal ALE is viewed as the reverse of atomic layer deposition (ALD).[28,29]

Thermal Al_2O_3 ALE using HF and $Al(CH_3)_3$ as the reactants is an example of thermal ALE using fluorination and ligand exchange.[16,19] HF is known to fluorinate Al_2O_3 to form an AlF_3

Received: January 5, 2019
Revised: March 21, 2019
Published: March 28, 2019

DOI: 10.1021/acs.jpcc.9b00124
J. Phys. Chem. C 2019, 123, 10346−10355

or AlF_xO_y layer on the Al_2O_3 surface.[16,19] The $Al(CH_3)_3$ then undergoes a ligand-exchange reaction with the fluorinated layer. $Al(CH_3)_3$ accepts fluorine from the fluorinated layer and donates methyl ligands to the surface. This ligand-exchange reaction allows the Al in the fluorinated Al_2O_3 layer to desorb as a volatile product. Recent quadrupole mass spectrometer studies have identified the etch product as $AlF(CH_3)_2$.[30] This etch product either appears as a dimer with itself ($AlF(CH_3)_2 \cdot AlF(CH_3)_2$) or with $Al(CH_3)_3$ ($AlF(CH_3)_2 \cdot Al(CH_3)_3$).[30]

This study explored the effect of the HF pressure on the Al_2O_3 etch rate during thermal Al_2O_3 ALE and the Al_2O_3 fluorination. The Al_2O_3 etch rates were determined using spectroscopic ellipsometry (SE) measurements. The fluoride layer thicknesses were measured using X-ray photoelectron spectroscopy (XPS). The time dependence and magnitude of the fluorination of Al_2O_3 were also examined using Fourier transform infrared (FTIR) vibrational studies. These studies help to understand HF fluorination of Al_2O_3 during Al_2O_3 ALE and the effect of the fluorination thickness on the Al_2O_3 etch rate.

This study also complements previous theoretical and experimental examinations of the fluorination of Al_2O_3. Earlier theoretical investigations have studied the fluorination of α-Al_2O_3 by HF using density functional theory (DFT) methods.[31,32] Recent theoretical investigations have also examined the fluorination of Θ-Al_2O_3 surfaces by HF and compared the fluorination to measured etch rates during Al_2O_3 ALE.[33] Many experimental studies have also explored the fluorination of Al_2O_3 because of the effect of fluorination on heterogeneous catalysis.[34,35] Fluorination is known to create strong Lewis acid sites that are important in a variety of reactions.

II. EXPERIMENTAL SECTION

II.A. Viscous and Static Flow Reactor. The ALD and ALE reactions were performed in a hot-walled, viscous, and static flow reactor.[36] A proportional-integral-derivative (PID) temperature controller (2604, Eurotherm) maintained the reactor temperatures of 200, 250, and 300 °C. The temperature was controlled to within ±0.04 °C of the set point. A bakeable capacitance manometer (Baratron 660A, MKS) monitored the reactor pressure.

ALD and ALE reactions were completed under static conditions in the reactor. Al_2O_3 ALD films were grown using sequential exposures of trimethylaluminum (TMA, 97% Sigma-Aldrich) and H_2O (Chromasolv for HPLC, Sigma-Aldrich) at 300 °C. Al_2O_3 ALE was performed using sequential exposures of HF derived from HF-pyridine (70 wt % HF, Sigma-Aldrich) and TMA as the reactants. A gold-plated stainless steel bubbler was used to contain the HF-pyridine and prevent corrosion. Ultra high purity (UHP) N_2 gas was used to purge the reactor between reactant exposures during ALD and ALE. UHP N_2 was delivered to the reactor via a mass flow controller at a flow rate of 200 sccm that produced a N_2 pressure of 1.0 Torr. The TMA, H_2O, and HF-pyridine precursors were all maintained at room temperature.

Static dosing was used for the ALD and ALE reactions. Before the precursors entered the reactor, the N_2 gas flow was stopped and the reactor was pumped down to the base pressure of ~30 mTorr. The reactor was then isolated from the mechanical pump and the reactant valves opened to allow the pressure to reach a partial pressure between 0.07 and 9.0 Torr. The reactant valves were closed after reaching the desired pressure. The pressures were held statically for 20 s for the ALD or ALE reactions. Viscous N_2 gas flows then purged the reactor for 20 s. Subsequently, the chamber was filled with N_2 with the gate valve closed and then the chamber was pumped down to the base pressure. This purging and pumping sequence after the reactant exposures was employed for both ALD and ALE reactions.

Al_2O_3 ALD films were grown on Si coupons using 200 Al_2O_3 ALD cycles and used as the substrates. Si(100) wafers (University Wafers) were cut into 1 cm × 1 cm coupons using a diamond scribe prior to the Al_2O_3 ALD. The Al_2O_3 film thicknesses were characterized using spectroscopic ellipsometery (SE). The initial Al_2O_3 ALD film thicknesses were between 18 and 20 nm.

II.B. *Ex Situ* Film Characterization Using Ellipsometry and XPS. The thickness of the Al_2O_3 film after ALD and ALE was measured using a spectroscopic ellipsometer (M-2000, J. A. Woollam). The spectroscopic ellipsometer had a spectral range from 240 to 1700 nm and utilized an incidence angle of 70°. The Ψ and Δ parameters were analyzed using a Cauchy model with the CompleteEASE software package (J. A. Woollam).

X-ray photoelectron spectroscopy (XPS) (PHI 5600, RBD Instruments) measured the film composition. A monochromatic Al Kα X-ray source (1486.6 eV) was used to collect survey scans with a pass energy of 93.9 eV and a step size of 0.400 eV. Auger Scan software package (Auger Scan, RBD Instruments) was employed to collect the data. Casa XPS software (Casa XPS, Casa Software) determined the surface concentrations using the peak areas for the C 1s, O 1s, Al 2p, and F 1s XPS signals and the corresponding sensitivity factors. All peak energies were calibrated to the adventitious C 1s peak centered at 284.8 eV.

II.C. *In Situ* Fourier Transform Infrared (FTIR) Spectroscopy. The fluorination of Al_2O_3 ALD films at 300 °C during sequential exposures of HF derived from HF-pyridine was studied using *in situ* FTIR spectroscopy. The *in situ* FTIR studies were performed in a reactor equipped with an FTIR spectrometer that has been described previously.[37] The FTIR experiments employed high surface area Si nanoparticles (>98%, US Research Nanomaterials) with an average diameter of 20−30 nm.

The Si nanoparticles were mechanically pressed into a tungsten grid to facilitate the transmission FTIR measurements. The tungsten grid was 2 × 3 cm^2, 50 μm thick, with 100 grid lines per inch. The tungsten grid was resistively heated using a DC power supply (6268B, 20V/20A, Hewlett-Packard). The voltage output of the power supply was controlled by a PID temperature controller (Love Controls 16B, Dwyer Instruments). A type K thermocouple was attached at the bottom of the tungsten grid with epoxy (Ceramabond 571, Aremco). The epoxy also electrically isolated the thermocouple from the tungsten grid.

The Al_2O_3 film was grown using Al_2O_3 ALD using TMA and H_2O. Both the TMA and H_2O precursors were maintained at room temperature. Subsequently, the tungsten grid was resistively heated to 300 °C and the Al_2O_3 ALD coating was exposed to HF at various pressures before recording the absorbance changes. The gold-coated bubbler for HF-pyridine was maintained at room temperature.

DOI: 10.1021/acs.jpcc.9b00124
J. Phys. Chem. C 2019, 123, 10346−10355

III. RESULTS AND DISCUSSION

III.A. Spectroscopic Ellipsometry Measurements of Thermal Al_2O_3 ALE. The Al_2O_3 ALD films were etched using HF and TMA at different reactant exposures and different temperatures. Both the HF and TMA reactants were at the same pressure. Figure 1 shows the Al_2O_3 thickness change after

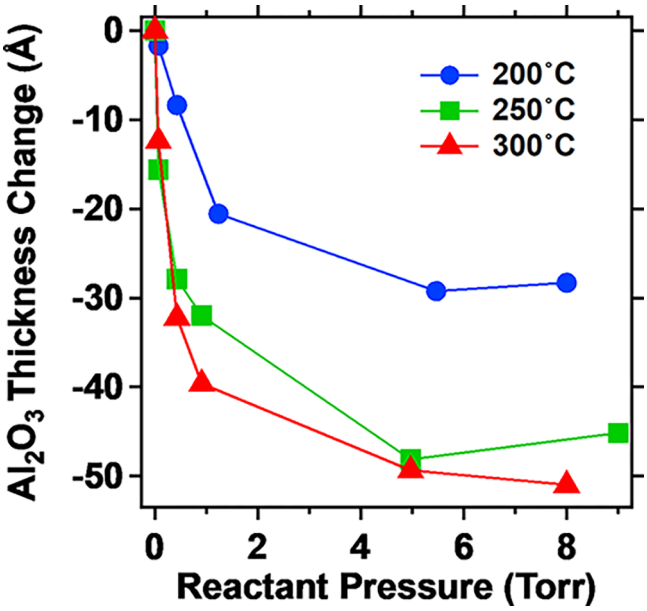

Figure 1. Al_2O_3 thickness change after 20 Al_2O_3 ALE cycles versus reactant pressure at 200, 250, and 300 °C.

20 ALE cycles using exposures of 20 s for HF and TMA followed by purging after each reactant exposure. The initial Al_2O_3 ALD film thickness was between 180 and 200 Å.

Figure 1 reveals that the Al_2O_3 thickness change after 20 ALE cycles is larger at both higher temperatures and higher HF pressures. The Al_2O_3 thickness changes vary more rapidly at the lower HF pressures. The Al_2O_3 thickness change after 20 ALE cycles begins to reach saturation values at the higher HF pressures. The Al_2O_3 thickness changes after 20 ALE cycles are larger at the higher temperatures in this saturation regime.

Figure 2 displays the Al_2O_3 etch rates corresponding to the Al_2O_3 thickness changes after 20 ALE cycles in Figure 1. The etch rates were calculated from the difference in the Al_2O_3 film thickness before and after ALE divided by the 20 ALE cycles. The Al_2O_3 etch rates are higher at higher reactant pressures. The higher temperatures also display higher Al_2O_3 etch rates. Similar results have been obtained earlier for the Al_2O_3 etch rate versus HF exposure and substrate temperature.[17] Figure 2 shows that the etch rates reach nearly self-limiting values at higher HF pressures. The Al_2O_3 etch rates are approximately 1.45, 2.30, and 2.50 Å/cycle at 200, 250, and 300 °C at higher HF pressures between 6 and 8 Torr.

The saturation behavior observed in Figures 1 and 2 suggests that the HF fluorination of Al_2O_3 reaches self-limiting fluoride thicknesses at higher HF pressures. This behavior is similar to the oxidation of silicon surfaces. For the same oxidation time during silicon oxidation, higher silicon oxide thicknesses are observed at higher O_2 pressures.[38,39] In addition, the silicon oxidation rates are progressively reduced at longer oxidation times in accordance with parabolic rate law behavior.[39] This silicon oxidation behavior is described by

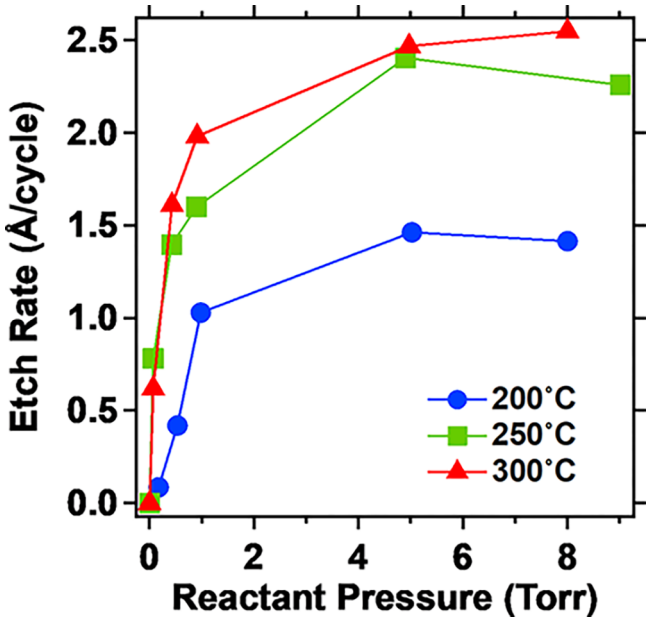

Figure 2. Al_2O_3 etch rate determined from results in Figure 1 versus reactant pressure at 200, 250, and 300 °C.

Deal–Grove oxidation kinetics.[40] A model for Al_2O_3 fluorination will be described later in section III.D.

III.B. XPS Measurement of Al_2O_3 Fluorination. XPS analysis was used to characterize the fluorination of Al_2O_3. Al_2O_3 ALD films on Si wafers were exposed to HF exposures for 30 s at HF pressures of 0.15, 1.0, 4.0, and 8.0 Torr at 300 °C. After the HF exposures, the samples were immediately transferred to the XPS chamber to minimize atmospheric exposure. High resolution scans were recorded that included the Al 2p, O 1s, F 1s, and C 1s XPS peaks. The XPS spectra were then evaluated using analysis software (CasaXPS) to determine the surface composition.

Figure 3 shows the atomic percentages from the Al 2p, O 1s, and F 1s peaks after the HF exposures for 30 s at HF pressures of 0, 0.15, 1.0, 4.0, and 8.0 Torr at 300 °C. Figure 3 reveals that the oxygen percentage decreases and the fluorine percentage increases at the higher HF pressures. In contrast, the aluminum percentage remains nearly constant for the various HF pressures. The loss of oxygen and the gain of fluorine are in agreement with the fluorination reaction to produce AlF_3 or AlF_xO_y. The reaction for AlF_3 production is $Al_2O_3 + 6HF \rightarrow 2AlF_3 + 3H_2O$. The reaction for AlF_xO_y production is $Al_2O_3 + zHF \rightarrow 2AlO_{(6-z)/4}F_{z/2} + (z/2)H_2O$.

The Al 2p XPS core-level spectrum of an initial Al_2O_3 ALD film is displayed in Figure 4a. The initial Al_2O_3 ALD film grown on a Si wafer is consistent with pristine Al_2O_3 with a peak at 74.3 eV and a full width at half-maximum (fwhm) of 2.0 eV. This peak serves as a calibration reference for the fluorinated Al_2O_3 samples. An Al_2O_3 ALD film after exposure to HF pressure for 30 s at 4.0 Torr at 300 °C is shown in Figure 4b.

The fluorination of Al_2O_3 leads to the growth of a higher energy shoulder in Figure 4b at a binding energy of 75.5 eV. This binding energy is lower than the reported binding energies of 77.3 and 77.5 eV for α-AlF_3 and β-AlF_3.[41] A binding energy for Al 2p that is intermediate between 74.3 eV for Al_2O_3 and 77.3–77.5 eV for AlF_3 is consistent with an aluminum oxyfluoride.[41,42] This aluminum oxyfluoride layer is

DOI: 10.1021/acs.jpcc.9b00124
J. Phys. Chem. C 2019, 123, 10346–10355

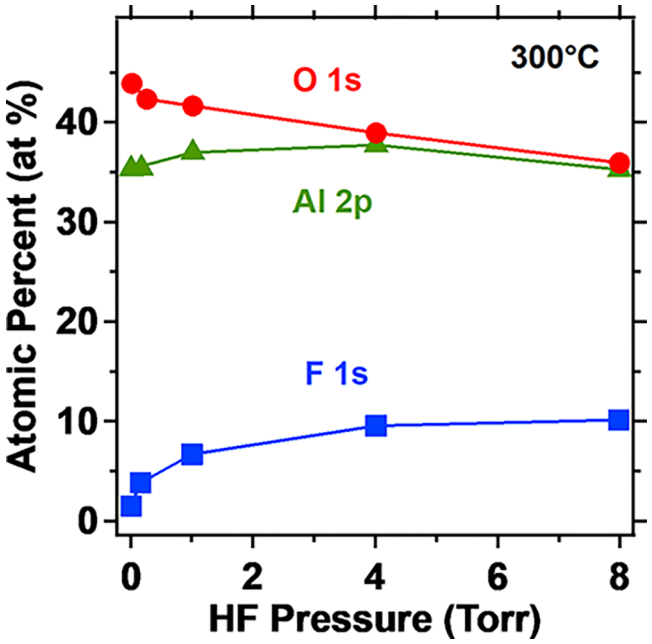

Figure 3. XPS measurement of atomic percent (atom %) of Al_2O_3 ALD film after HF exposures at various HF pressures for 30 s at 300 °C.

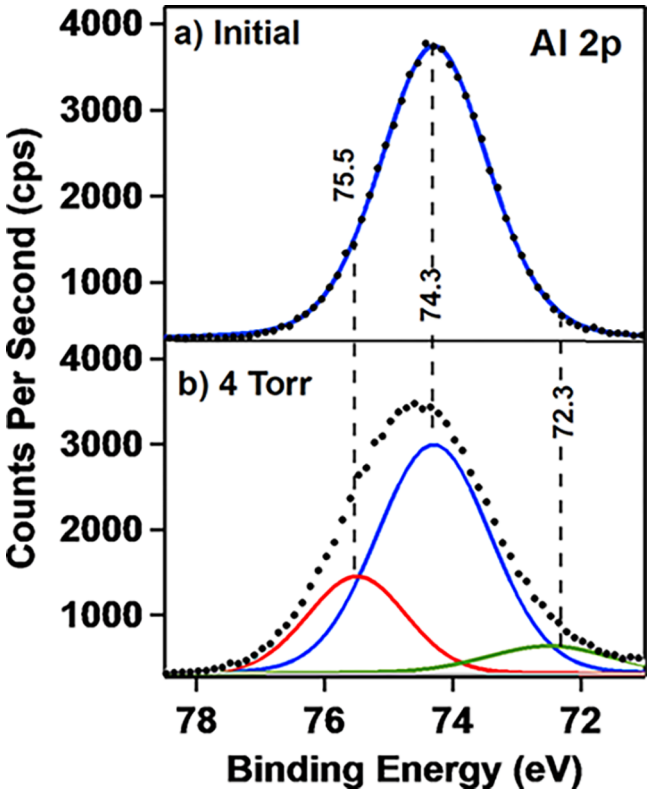

Figure 4. High resolution scan of the Al 2p XPS peak for (a) initial Al_2O_3 ALD film and (b) Al_2O_3 ALD film after HF exposure for 30 s at 4 Torr and 300 °C.

consistent with recent theoretical calculations of the aluminum fluoride layer on the surface of Θ-Al_2O_3 after HF exposures.[33] HF exposure to Θ-Al_2O_3 produced a dissociated F coverage of 7.1 ± 0.3 F/nm^2 after saturation HF exposures.[33] This F coverage is consistent with 1.5 F atoms bound to each surface Al atom.[33]

Some Al 2p XPS peak intensity also shifts to lower energies. Fitting of this shoulder at lower energy requires the addition of a small XPS peak at 72.3 eV. An Al 2p XPS peak at 72.3 eV is consistent with metallic aluminum.[42,43] This apparent reduction may result from the presence of H_2 in the HF. The H_2 is formed when HF is in contact with the stainless-steel walls of the gas lines for extended times. Mass spectrometer experiments confirmed that HF slowly reacts with the stainless-steel walls and produces H_2. This H_2 could then lead to the reduction of Al_2O_3, AlO_xF_y, or AlOH species during the initial HF exposure at 300 °C. However, this explanation is speculative because thermochemical calculations indicate that H_2 reduction of Al_2O_3, AlF_3, or $Al(OH)_3$ is not favorable.

III.C. Determination of Fluoride Layer Thickness. The thickness of the fluoride layer was also determined using XPS measurements. The sample was assumed to have a uniform layered structure composed of an Al_2O_3 substrate, an aluminum fluoride layer of varying thickness, and a 6 Å thick adventitious carbon layer at the sample−air interface.[44] The XPS results in Figure 4b indicate that the fluoride layer is an aluminum oxyfluoride. However, the exact composition of the aluminum oxyfluoride is not known. This XPS analysis considered fluoride layers with compositions of AlF_3, Al_2OF_4, and AlOF. The analysis assuming an aluminum oxyfluoride with a composition of Al_2OF_4 is given below.

The XPS electrons are derived from the C, Al, F, and O in the three layers. XPS quantification requires analysis of the attenuation of photoelectron propagation in their source layers. In addition, the photoelectron propagation is also attenuated by each layer that covers the source layer.[45,46] For example, the C signal is derived from the top adventitious carbon layer.[44] The C photoelectrons will be attenuated by propagation in the carbon layer according to $\exp[-t/\lambda_C]$, where t is the thickness of the carbon layer at the source of the C photoelectron and λ_C = 30.2 Å is the inelastic mean free path (IMFP) of the C XPS photoelectron at 1202 eV in the carbon layer.[47]

The C XPS signal is proportional to ρ_c, the carbon number density in the carbon layer times the integral of $\exp[-t/\lambda_C]$ from 0 to 6 Å.[44] This integral describes the effect of attenuation by the carbon layer on all of the C XPS electrons from various thicknesses in the carbon layer. The intensity of the C XPS signal is

$$I_C = \rho_C \int_0^6 e^{-t/\lambda_C}\, dt \quad (1)$$

The fluorine signal is derived from F in the Al_2OF_4 layer under the carbon layer. The F signal is proportional to ρ_{F,Al_2OF_4}, the fluorine number density in the Al_2OF_4 layer, times the integral of $\exp[-t/\lambda_F]$ from 0 to t_F, the thickness of the Al_2OF_4 layer. This integral describes the effect of attenuation by the Al_2OF_4 layer on the F XPS electrons. λ_F = 27.1 Å is the inelastic mean free path (IMFP) for the F XPS electrons at 801 eV.[47] The F XPS electrons are then attenuated by the overlying carbon layer. The intensity of the F XPS signal is

$$I_F = \rho_{F,Al_2OF_4} e^{-6/\lambda_F} \int_0^{t_F} e^{-t/\lambda_F}\, dt \quad (2)$$

The aluminum signal is derived from Al in the Al_2O_3 and Al in the Al_2OF_4 layer under the carbon layer. For the Al in the Al_2O_3 layer, the Al signal is proportional to ρ_{Al,Al_2O_3} the

DOI: 10.1021/acs.jpcc.9b00124
J. Phys. Chem. C 2019, 123, 10346−10355

aluminum number density in the Al_2O_3 layer times the integral of $\exp[-t/\lambda_{Al,Al_2O_3}]$ from 0 to ∞. For the Al in the Al_2OF_4 layer, the Al signal is proportional to ρ_{Al,Al_2OF_4}, the aluminum number density in the Al_2OF_4 layer times the integral of $\exp[-t/\lambda_{Al,Al_2OF_4}]$ from 0 to t_F, the thickness of the Al_2OF_4 layer. $\lambda_{Al,Al_2O_3} = \lambda_{Al,Al_2OF_4} = 27.7$ Å is the inelastic mean free path (IMFP) of the Al XPS electrons at 1412 eV.[48] The intensity of the Al XPS signal is

$$I_{Al} = \rho_{Al,Al_2OF_4} e^{-6/\lambda_{Al}} \int_0^{t_F} e^{-t/\lambda_{Al}}\, dt + \rho_{Al,Al_2O_3} e^{-6/\lambda_{Al}} e^{-t_F/\lambda_{Al}} \int_0^{\infty} e^{-t/\lambda_{Al}}\, dt \quad (3)$$

Lastly, the oxygen signal is derived from O in the Al_2O_3 layer under the carbon and Al_2OF_4 layers. $\lambda_O = 20.5$ Å is the inelastic mean free path (IMFP) for the O XPS electrons at 956 eV.[48] Following a similar treatment, the intensity of the O XPS signal is

$$I_O = \rho_{O,C} \int_0^{6} e^{-t/\lambda_O}\, dt + \rho_{O,Al_2OF_4} e^{-6/\lambda_O} \int_0^{t_F} e^{-t/\lambda_O} + \rho_{O,Al_2O_3} e^{-6/\lambda_O} e^{-t_F/\lambda_O} \int_0^{\infty} e^{-t/\lambda_O} \quad (4)$$

The total XPS signal is the sum of all of the individual XPS electrons produced by the Al_2O_3, Al_2OF_4, and carbon layers and their attenuation during propagation. The thickness of the Al_2OF_4 layer was determined by varying t_F and determining the t_F value that was consistent with the observed C, Al, F, and O XPS signals. The number density for carbon in the adventitious carbon was 5×10^{22} cm^{-3}. The number densities for Al, F, and O in the Al_2OF_4 layer were 2.5×10^{22}, 4.9×10^{22}, and 1.2×10^{22} cm^{-3}, respectively. The number densities for Al and O in the Al_2O_3 substrate were 3.66×10^{22} and 5.5×10^{22} cm^{-3}, respectively.

The thickness of the Al_2OF_4 layer as a function of HF pressure determined by the XPS measurements is displayed in Figure 5. The Al_2OF_4 fluoride layer thicknesses were 2.0, 3.5, 5.2, and 5.5 Å for HF pressures of 0.15, 1.0, 4.0, and 8.0 Torr, respectively. XPS analysis assuming fluoride layers with compositions of AlF_3 and AlOF yielded fluoride thicknesses with a similar functional form versus HF pressure to the results shown in Figure 5. However, the absolute fluoride thicknesses varied for the different aluminum fluorides. At an HF pressure of 8 Torr, the fluoride thicknesses were 4.5, 5.5, and 10.2 Å when the aluminum fluoride layer was assumed to be AlF_3, Al_2OF_4, and AlOF, respectively.

Figure 5 also compares the fluoride layer thicknesses with the Al_2O_3 etch rates obtained at the same HF pressures. The TMA pressure during the Al_2O_3 ALE was equivalent to the HF pressure. Figure 5 shows that there is excellent correspondence between the fluoride layer thicknesses and the Al_2O_3 etch rates. This correlation argues that the ligand-exchange reaction between TMA and the aluminum fluoride layer during Al_2O_3 ALE is removing Al_2O_3 at a rate that is proportional to the aluminum fluoride thickness.

Figure 6 shows the Al_2O_3 etch rate versus the fluoride layer thickness for reactant pressures between 0 and 8.0 Torr. The reactant pressures correspond to both the HF and TMA pressures during Al_2O_3 ALE. Higher reactant pressures increase both the fluoride layer thickness and the Al_2O_3 etch rate. The linear relationship between the etch rate and fluoride

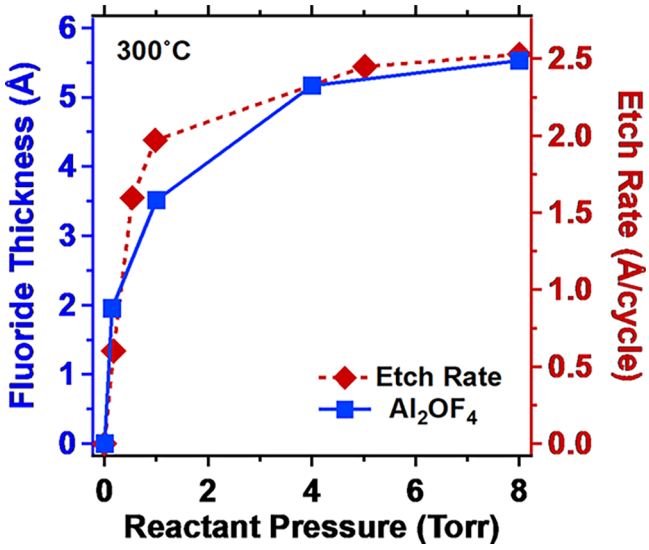

Figure 5. Comparison of fluoride thickness and etch rate during Al_2O_3 ALE versus reactant pressure. Fluoride thickness was measured by XPS analysis assuming a composition of Al_2OF_4 after HF exposure for 30 s at 300 °C. Etch rate was measured for Al_2O_3 ALE at 300 °C using reactant exposures of 30 s at various reactant pressures.

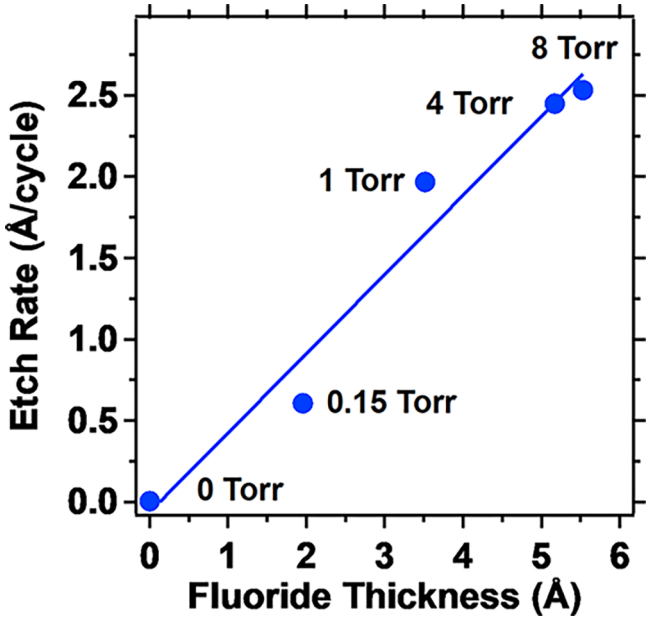

Figure 6. Correlation of etch rate for Al_2O_3 ALE and fluoride thickness assuming a composition of Al_2OF_4 for various reactant pressures.

layer again indicates that the etch rate is proportional to the thickness of the fluoride layer.

III.D. FTIR Spectroscopy Measurements of Al_2O_3 Fluorination. FTIR spectroscopy was also used to monitor the fluorination of Al_2O_3. These fluorination experiments could be performed *in situ* without atmospheric exposures after the fluorination. Figure 7 shows the original Al_2O_3 ALD film and the same Al_2O_3 ALD film after subsequent consecutive HF exposures at 0.5 Torr under static conditions with the gate valve closed to the pump. The HF pressure was held for 15 s before purging the reactor. Results are displayed after 2, 4, 6, 8, and 10 HF exposures.

DOI: 10.1021/acs.jpcc.9b00124
J. Phys. Chem. C 2019, 123, 10346−10355

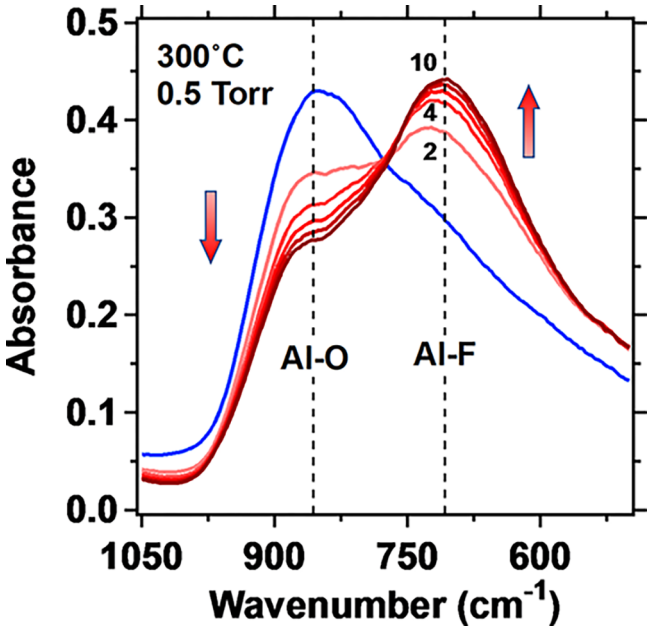

Figure 7. Absorbance for Al−O and Al−F stretching vibrations during fluorination of Al_2O_3 by HF pressure at 300 °C. Consecutive HF exposures were defined by a HF pressure of 0.5 Torr for 15 s.

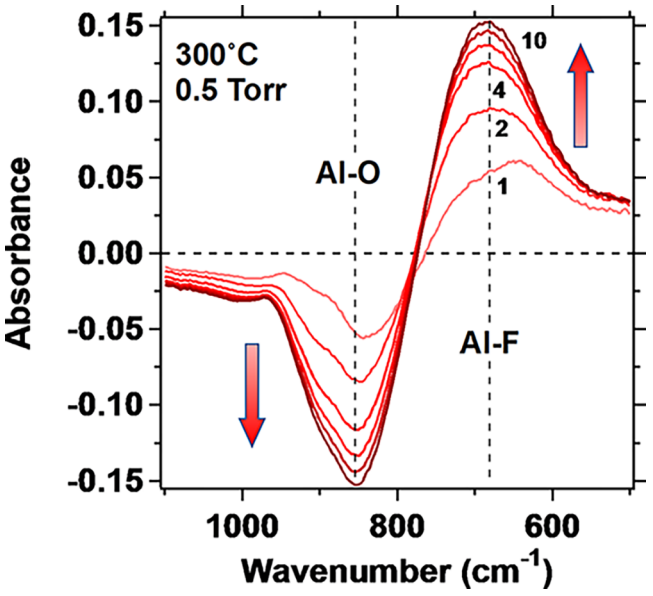

Figure 8. Difference spectra showing the absorbance of Al−O and Al−F stretching vibrations during fluorination of Al_2O_3 by HF at 300 °C. Consecutive HF exposures were defined by a HF pressure of 0.5 Torr for 15 s.

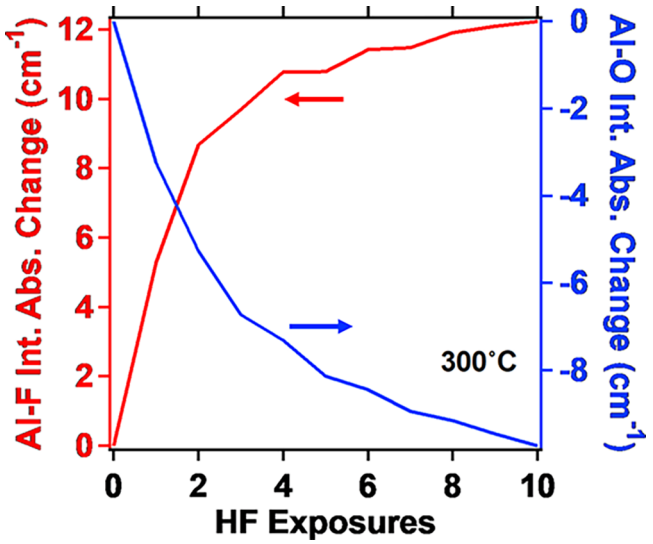

Figure 9. Integrated absorbance change for Al−F and Al−O stretching vibrations versus HF exposures at 300 °C determined from the difference spectra in Figure 8. Each HF exposure was defined by a HF pressure of 0.5 Torr for 15 s.

The absorbance peak at 850 cm^{-1} corresponds with the Al−O stretching vibration in Al_2O_3.[49] The absorbance peak at 700 cm^{-1} corresponds to the Al−F stretching vibration in AlF_3 or AlF_xO_y.[16] The absorbance progressively converts between Al−O stretching vibrations to Al−F stretching vibrations versus the consecutive HF exposures. The absorbance for the Al−O stretching vibration is reduced and the absorbance for the Al−F stretching vibrations is increased versus HF exposures. These results are consistent with the conversion of Al_2O_3 to AlF_3 or AlO_xF_y by the reactions $Al_2O_3 + 6HF \rightarrow 2AlF_3 + 3H_2O$ or $Al_2O_3 + zHF \rightarrow 2AlO_{(6-z)/4}F_{z/2} + (z/2)H_2O$.

An apparent isosbestic point exists in Figure 7 between the absorbance peaks for the Al−O and Al−F stretching vibrations. The isosbestic point occurs at 779 cm^{-1}. This isosbestic point argues for direct conversion of the aluminum oxide to aluminum fluoride. The Al−O and Al−F vibrations act nearly separately and independently of each other as the Al_2O_3 film is progressively fluorinated.

Figure 8 shows the difference spectra versus sequential HF exposures at 0.5 Torr and 300 °C for 15 s. The results are shown after 1, 2, 4, 6, 8, and 10 HF exposures. These difference spectra are all referenced to the initial Al_2O_3 ALD film on the silicon particles. The absorbance loss for the Al−O stretching vibration is centered at 850 cm^{-1}, and the absorbance gain for the Al−F stretching vibration is centered at 700 cm^{-1}. The isosbestic point between the gain and loss of the absorbance peaks again occurs at 779 cm^{-1}.

Difference spectra facilitate the determination of the integrated absorbance change of the Al−O and Al−F stretching vibrations versus HF exposure. Figure 9 shows the integrated absorbance change of the Al−O and Al−F stretching vibrations. The integrated absorbance changes were defined from the difference spectra displayed in Figure 8. Integration was performed from the isosbestic point to 1100 cm^{-1} for the Al−O stretching vibration and from 500 to the isosbestic point for the Al−F stretching vibration. There is a correlation between the loss of absorbance for the Al−O stretching vibration and gain of absorbance for the Al−F stretching vibrations with HF exposure. Similar behavior was observed in Figure 3 when monitoring the XPS O 1s and F 1s peaks.

The conversion of aluminum oxide to aluminum fluoride is also dependent on the HF pressure. Figure 10 shows the initial spectrum for Al_2O_3 obtained after 15 cycles of Al_2O_3 ALD at 155 °C referenced to the Si particles. The spectra are also shown for the Al_2O_3 ALD film after static HF exposures at 0.5 and 4.0 Torr, respectively. The spectra were recorded after six HF exposures for 15 s at both pressures at 300 °C. After the six HF exposures, the spectra have nearly reached saturation levels where the absorbance changes become negligible with subsequent HF exposures. The results in Figure 10 indicate

DOI: 10.1021/acs.jpcc.9b00124
J. Phys. Chem. C 2019, 123, 10346−10355

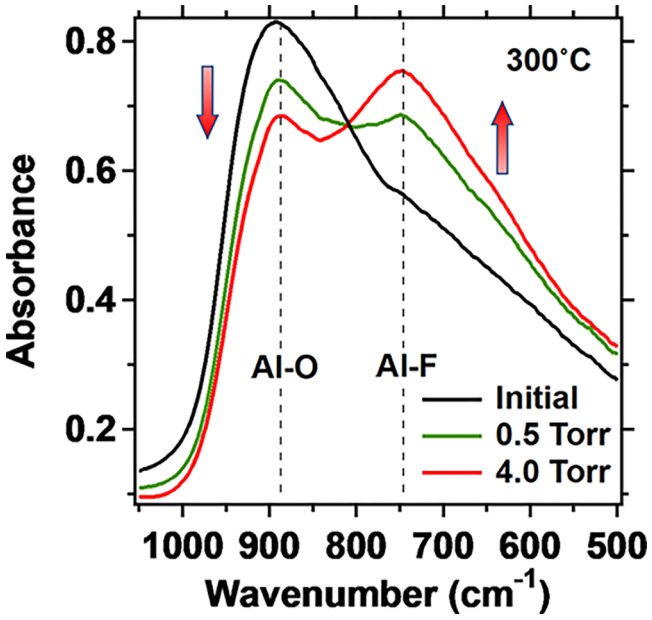

Figure 10. Absorbance for Al−O and Al−F stretching vibrations during the fluorination of Al_2O_3 by HF at 300 °C. HF exposures were defined by HF pressures of 0.5 Torr and then 4.0 Torr for 15 s.

that the HF pressure increases the saturation level for the fluorination of Al_2O_3.

Figure 11 shows the difference spectra versus sequential HF exposures for 15 s at 4 Torr and 300 °C. The results are shown

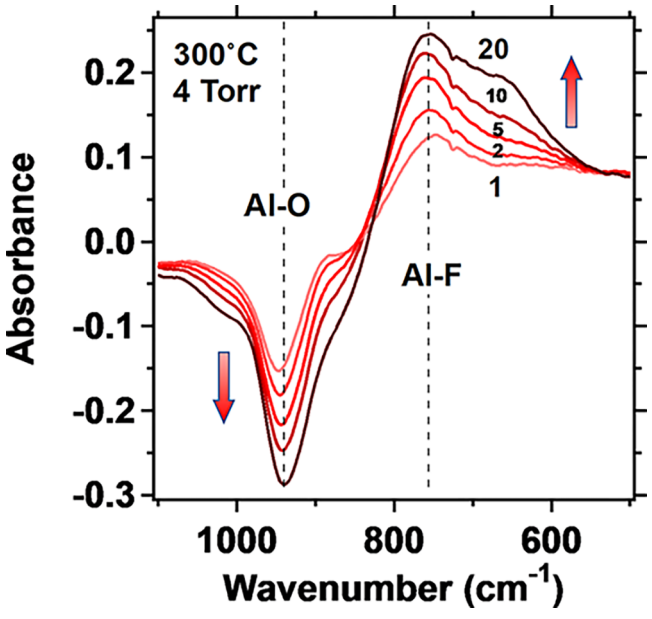

Figure 11. Difference spectra showing absorbance of Al−O and Al−F stretching vibrations during fluorination of Al_2O_3 by HF at 300 °C. Consecutive HF exposures were defined by a HF pressure of 4.0 Torr for 15 s.

after 1, 2, 5, 10, and 20 HF exposures. The absorbance loss for the Al−O stretching vibration is centered at 940 cm^{-1}, and the absorbance gain for the Al−F stretching vibration is peaked at 760 cm^{-1}. The absorbance changes at 4 Torr in Figure 11 are larger than the absorbance changes at 0.5 Torr in Figure 8. In addition, the frequencies of the absorbance loss and gain are shifted to higher frequencies at HF pressures of 4 Torr.

The higher frequencies for the absorbance loss and gain at HF pressures of 4 Torr may be related to the vibrations lost and gained versus HF pressure. At low HF pressures of 0.5 Torr, the fluoride thickness is ∼2.5 Å according to Figure 5 and fluorination is more confined to the Al_2O_3 surface region. At higher HF pressures of 4 Torr, the fluoride thickness is ∼5.2 Å according to Figure 5 and the fluorination occurs deeper into the Al_2O_3 bulk. Al−O bonds in the surface region that are lost during fluorination may have lower frequencies than the Al−O bonds located further into the Al_2O_3 bulk. Likewise, the Al−F bonds formed in the surface region may have lower frequencies than the Al−F bonds that are formed deeper into the Al_2O_3 bulk. As a result of these frequency shifts with HF pressure, the isosbestic points were also dependent on HF pressure. The isosbestic points were 779, 836, 840, and 842 cm^{-1} for HF pressures of 0.5, 1.0, 4.0, and 8.0 Torr, respectively.

Figure 12 shows the integrated absorbance change of the Al−F stretching vibration as a function of HF exposures for HF

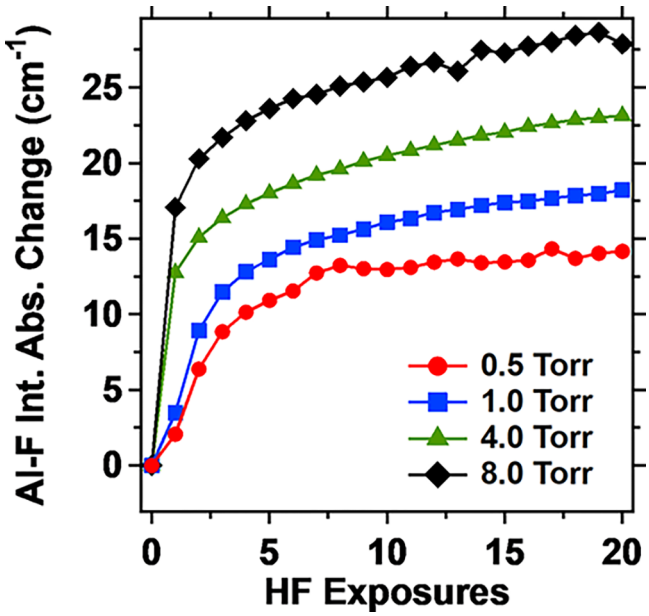

Figure 12. Integrated absorbance change for Al−F stretching vibrations during fluorination of Al_2O_3 by HF at 300 °C. HF pressure was varied from 0.5 to 8.0 Torr. Each HF exposure was performed for 15 s.

pressures of 0.5, 1.0, 4.0, and 8.0 Torr. This integrated absorbance change was defined from 500 cm^{-1} to the isosbestic point for the difference spectra at various HF pressures. The integrated absorbance change initially increases rapidly for the first several HF exposures. The integrated absorbance change then begins to level off after multiple HF exposures. The saturation levels are dependent on the HF pressure. Higher HF pressures produce larger integrated absorbance changes for the Al−F stretching vibrations.

Figure 13 shows the integrated absorbance change for the Al−F stretching vibration as a function of HF exposure in units of Torr s. These results illustrate that HF exposure defines the initial integrated absorbance change independent of the actual HF pressure. This regime is associated with the fluorination of the Al_2O_3 surface. At an integrated absorbance change >10 cm^{-1}, the integrated absorbance change is somewhat depend-

DOI: 10.1021/acs.jpcc.9b00124
J. Phys. Chem. C 2019, 123, 10346−10355

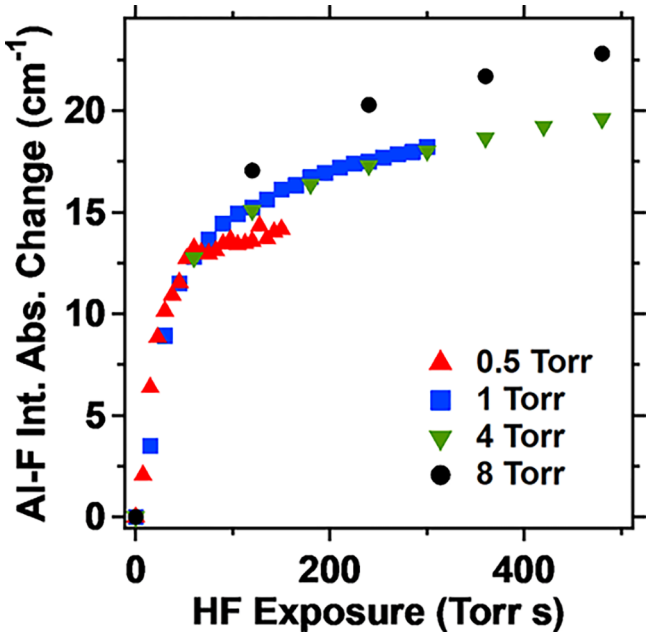

Figure 13. Integrated absorbance change for Al−F stretching vibrations versus HF exposure in units of Torr s during the fluorination of Al_2O_3 by HF at 300 °C. HF pressure was varied from 0.5 to 8.0 Torr.

ent on the HF pressure. HF exposures obtained using higher HF pressures have slightly higher integrated absorbance changes.

III.E. Mechanism for Fluorination of Al_2O_3. The results in Figures 12 and 13 suggest a mechanism for Al_2O_3 fluorination based on rapid fluorination of the Al_2O_3 surface and then slower fluorination of the near surface region. The Al_2O_3 surface is fluorinated on the basis of site availability consistent with Langmuir adsorption. The rate of surface fluorination is expected to follow Langmuir adsorption kinetics given by $d\Theta/dt = b(1 - \Theta_s)$, where b is a rate constant that is proportional to HF pressure and Θ_s is the saturated fluorine coverage. Integration of this rate equation predicts that $\Theta(t) = \Theta_s[1 - \exp(-bt)]$.

In comparison, fluorination of the near surface region is expected to produce a fluoride thickness, x, that grows according to $dx/dt = k/x$. k is a constant that is dependent on the HF pressure, $k = k_0P$. The inverse dependence of dx/dt on x is consistent with a fluoride thickness that acts as a diffusion barrier for subsequent fluorination. Integration of this rate equation yields $x(t)^2 = 2kt$. This equation is known as the parabolic law.[50]

Mathematically combining the surface and near surface fluorination rates into one composite expression is difficult. An approximation that allows for derivation of a composite solution assumes that the surface fluorination rate can be treated as $dx/dt = ck/x(\exp(-t/\tau))$, where c is a constant and τ is inversely proportional to the HF pressure, $\tau = \tau_0/P$. Integration of this rate equation yields $x(t)^2 = ck\tau[1 - \exp(-t/\tau)]$. This integrated rate equation is similar in form to the integration of the Langmuir adsorption rate expression. However, the square of the fluoride thickness is present instead of the linear fluorine coverage.

Treating the surface fluorination as $dx/dt = ck/x(\exp(-t/\tau))$ leads to a composite expression for the surface and near surface fluorination rates:

$$\frac{dx}{dt} = \frac{k}{x}[1 + ce^{-t/\tau}] \quad (5)$$

After rearrangement, the integrals can be written as

$$\int_0^x x'\,dx' = k\int_0^t (1 - ce^{-t'/\tau})\,dt' \quad (6)$$

Solving these integrals then leads to the expression for the fluoride thickness, x,

$$x(t)^2 = 2kt + M(1 - e^{-t/\tau}) \quad (7)$$

where $M = 2kc\tau$. The pressure dependence for $x(t)^2$ given by eq 7 can then be highlighted by substituting for $k = k_0P$ and $\tau = \tau_0/P$. These substitutions yield

$$x(t)^2 = (k_0P)t + M(1 - e^{-Pt/\tau_0}) \quad (8)$$

Assuming that the Al−F integrated absorbance change measures the Al_2O_3 fluorination, eq 8 can be used to fit the experimental results. Figure 14 shows the fits for $x(t)^2$ in eq 8

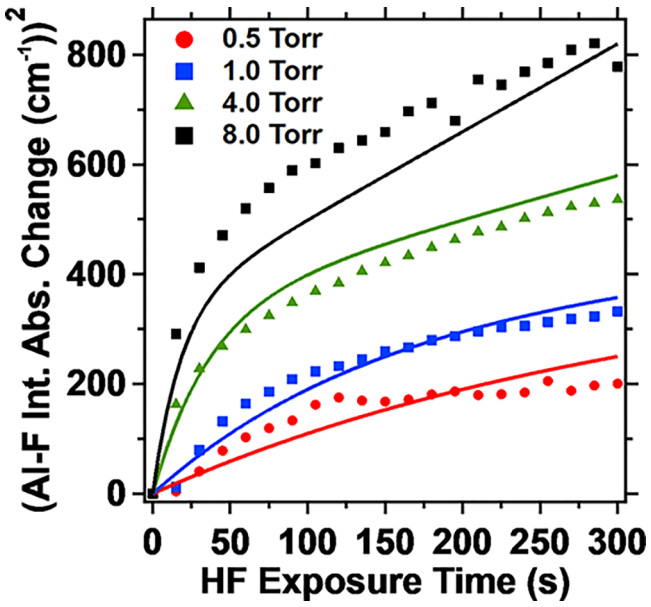

Figure 14. Comparison of $x(t)^2$ given by eq 8 for square of fluoride thickness versus time for different HF pressures to square of Al−F integrated absorbance change versus HF exposure time at different HF pressures.

to the square of the Al−F integrated absorbance change for HF pressures of 0.5, 1.0, 4.0, and 8.0 Torr. These fits used constant values of $k_0 = 0.2$ $(cm^{-1})^2/(Torr\ s)$, $M = 340$ $(cm^{-1})^2$, and $\tau_0 = 144(Torr\ s)$ for all of the HF pressures. k_0 and M have units of $(cm^{-1})^2$ because $x(t)^2$ in eq 8 was fit to the Al−F integrated absorbance change in units of $(cm^{-1})^2$.

The $x(t)^2$ fits are in approximate agreement with the experimental data for the square of the Al−F integrated absorbance change for the various HF pressures. Equation 8 is close to capturing the pressure dependence in the surface and near surface fluorination rates of Al_2O_3. The initial fluorination of the Al_2O_3 surface is faster at the higher HF pressures. In addition, the magnitude of fluorination of the Al_2O_3 near surface region is also dependent on the HF pressure and displays the linear increase expected from the parabolic law.

This mechanism for the fluorination of Al_2O_3 is similar to the mechanism for silicon oxidation.[40,51] For both systems,

DOI: 10.1021/acs.jpcc.9b00124
J. Phys. Chem. C 2019, 123, 10346−10355

there are rapid surface kinetics followed by slower parabolic law kinetics for the near surface region. The surface kinetics can be understood in terms of surface site availability. The kinetics for the near surface region can be described according to transport through a growing diffusion barrier on the surface. Higher pressures provide a larger coverage gradient for transport through the surface diffusion barrier.

IV. CONCLUSIONS

Thermal Al_2O_3 ALE can be achieved using a fluorination and ligand-exchange mechanism with HF and TMA as the reactants. This study explored the effect of HF pressure on the Al_2O_3 etching rate and Al_2O_3 fluorination. Using *ex situ* SE measurements, the Al_2O_3 etch rates at different temperatures were observed to increase with HF pressures and then level out at higher HF pressures. At 300 °C, Al_2O_3 etch rates of 0.6, 1.6, 2.0, 2.4, and 2.5 Å/cycle were measured for HF pressures of 0.17, 0.5, 1.0, 5.0, and 8.0 Torr, respectively. Assuming an Al_2OF_4 layer on the Al_2O_3 surface, the estimated fluoride thicknesses on Al_2O_3 also increased with HF pressures and reached saturation values at higher HF pressures. Fluoride thicknesses on Al_2O_3 of 2.0, 3.5, 5.2, and 5.5 Å were obtained for HF pressures of 0.15, 1.0, 4.0, and 8.0 Torr, respectively, at 300 °C. There was a very good correlation between the Al_2O_3 etch rates and the fluoride layer thicknesses versus HF pressure.

The time dependence and magnitude of the Al_2O_3 fluorination were also analyzed using *in situ* FTIR vibrational studies by monitoring the infrared absorbance from the Al−O and Al−F stretching vibrations. The time dependence of the Al_2O_3 fluorination was understood by a mechanism involving the rapid fluorination of the Al_2O_3 surface at initial HF exposures and slower fluorination into the Al_2O_3 near surface region that begins to level off at longer HF exposure times. The pressure dependence of the Al_2O_3 fluorination was explained by facile adsorption on the initial available sites on the Al_2O_3 surface. This rapid fluorination is followed by slower diffusion into the near surface region of Al_2O_3 where the fluoride layer serves as a diffusion barrier to subsequent fluorination.

The fluoride layer acts as a diffusion barrier and yields parabolic law behavior. The higher HF pressures provide a higher coverage gradient for transport through the diffusion barrier and yield larger fluoride thicknesses for equal fluorination times. A kinetic model was developed that combined the rates of surface and near surface fluorination. The integration of the combined kinetic rate law yielded a solution for the fluoride thickness versus time as a function of HF pressure. This solution for the square of the fluoride thickness was in good agreement with the experimental results for the square of the Al−F integrated absorbance change for the various HF pressures.

AUTHOR INFORMATION

Corresponding Author

*E-mail: Steven.George@Colorado.edu.

ORCID

Steven M. George: 0000-0003-0253-9184

Notes

The authors declare no competing financial interest.

ACKNOWLEDGMENTS

This research was funded by the National Science Foundation (CHE-1609554). The authors thank Dr. Huaxing Sun for recording the XPS results.

REFERENCES

(1) Kanarik, K. J.; Lill, T.; Hudson, E. A.; Sriraman, S.; Tan, S.; Marks, J.; Vahedi, V.; Gottscho, R. A. Overview of Atomic Layer Etching in the Semiconductor Industry. *J. Vac. Sci. Technol., A* **2015**, *33*, 020802.

(2) Matsuura, T.; Murota, J.; Sawada, Y.; Ohmi, T. Self-Limited Layer-by-Layer Etching of Si by Alternated Chlorine Adsorption and Ar^+ Ion Irradiation. *Appl. Phys. Lett.* **1993**, *63*, 2803−2805.

(3) Park, S. D.; Lee, D. H.; Yeom, G. Y. Atomic Layer Etching of Si(100) and Si(111) Using Cl_2 and Ar Neutral Beam. *Electrochem. Solid-State Lett.* **2005**, *8*, C106−C109.

(4) Sakaue, H.; Iseda, S.; Asami, K.; Yamamoto, J.; Hirose, M.; Horiike, Y. Atomic Layer Controlled Digital Etching of Silicon. *Jpn. J. Appl. Phys. 1* **1990**, *29*, 2648−2652.

(5) Sugiyama, T.; Matsuura, T.; Murota, J. Atomic-Layer Etching of Ge Using an Ultraclean ECR Plasma. *Appl. Surf. Sci.* **1997**, *112*, 187−190.

(6) Lim, W. S.; Park, S. D.; Park, B. J.; Yeom, G. Y. Atomic Layer Etching of (100)/(111) GaAs with Chlorine and Low Angle Forward Reflected Ne Neutral Beam. *Surf. Coat. Technol.* **2008**, *202*, 5701−5704.

(7) Metzler, D.; Bruce, R. L.; Engelmann, S.; Joseph, E. A.; Oehrlein, G. S. Fluorocarbon Assisted Atomic Layer Etching of SiO_2 Using Cyclic Ar/C_4F_8 Plasma. *J. Vac. Sci. Technol., A* **2014**, *32*, 020603.

(8) Metzler, D.; Li, C.; Engelmann, S.; Bruce, R. L.; Joseph, E. A.; Oehrlein, G. S. Fluorocarbon Assisted Atomic Layer Etching of SiO_2 and Si Using Cyclic Ar/C_4F_8 and Ar/CHF_3 Plasma. *J. Vac. Sci. Technol., A* **2016**, *34*, 01b101.

(9) Park, J. B.; Lim, W. S.; Park, B. J.; Park, I. H.; Kim, Y. W.; Yeom, G. Y. Atomic Layer Etching of Ultra-Thin HfO_2 Film for Gate Oxide in MOSFET Sevices. *J. Phys. D: Appl. Phys.* **2009**, *42*, 055202.

(10) Li, C.; Metzler, D.; Lai, C. S.; Hudson, E. A.; Oehrlein, G. S. Fluorocarbon Based Atomic Layer Etching of Si_3N_4 and Etching Selectivity of SiO_2 Over Si_3N_4. *J. Vac. Sci. Technol., A* **2016**, *34*, 041307.

(11) Kim, Y. Y.; Lim, W. S.; Park, J. B.; Yeom, G. Y. Layer by Layer Etching of the Highly Oriented Pyrolythic Graphite by Using Atomic Layer Etching. *J. Electrochem. Soc.* **2011**, *158*, D710−D714.

(12) Vogli, E.; Metzler, D.; Oehrlein, G. S. Feasibility of Atomic Layer Etching of Polymer Material Based on Sequential O_2 Exposure and Ar Low-Pressure Plasma-Etching. *Appl. Phys. Lett.* **2013**, *102*, 253105.

(13) Lee, Y.; George, S. M. Atomic Layer Etching of Al_2O_3 Using Sequential, Self-Limiting Thermal Reactions with $Sn(acac)_2$ and HF. *ACS Nano* **2015**, *9*, 2061−2070.

(14) George, S. M.; Lee, Y. Prospects for Thermal Atomic Layer Etching Using Sequential, Self-Limiting Fluorination and Ligand-Exchange Reactions. *ACS Nano* **2016**, *10*, 4889−4894.

(15) Lee, Y.; George, S. M. Thermal Atomic Layer Etching of Titanium Nitride Using Sequential, Self-Limiting Reactions: Oxidation to TiO_2 and Fluorination to Volatile TiF_4. *Chem. Mater.* **2017**, *29*, 8202−8210.

(16) DuMont, J. W.; George, S. M. Competition Between Al_2O_3 Atomic Layer Etching and AlF_3 Atomic Layer Deposition Using Sequential Exposures of Trimethylaluminum and Hydrogen Fluoride. *J. Chem. Phys.* **2017**, *146*, 052819.

(17) Hennessy, J.; Moore, C. S.; Balasubramanian, K.; Jewell, A. D.; France, K.; Nikzad, S. Enhanced Atomic Layer Etching of Native Aluminum Oxide for Ultraviolet Optical Applications. *J. Vac. Sci. Technol., A* **2017**, *35*, 041512.

(18) Lee, Y.; DuMont, J. W.; George, S. M. Mechanism of Thermal Al_2O_3 Atomic Layer Etching Using Sequential Reactions with $Sn(acac)_2$ and HF. *Chem. Mater.* **2015**, *27*, 3648−3657.

DOI: 10.1021/acs.jpcc.9b00124
J. Phys. Chem. C 2019, 123, 10346−10355

(19) Lee, Y.; DuMont, J. W.; George, S. M. Trimethylaluminum as the Metal Precursor for the Atomic Layer Etching of Al_2O_3 Using Sequential, Self-Limiting Thermal Reactions. *Chem. Mater.* **2016**, *28*, 2994−3003.
(20) Lee, Y.; DuMont, J. W.; George, S. M. Atomic Layer Etching of HfO_2 Using Sequential, Self-Limiting Thermal Reactions with $Sn(acac)_2$ and HF. *ECS J. Solid State Sci. Technol.* **2015**, *4*, N5013−N5022.
(21) Lee, Y.; George, S. M. Thermal Atomic Layer Etching of HfO_2 Using HF for Fluorination and $TiCl_4$ for Ligand-Exchange. *J. Vac. Sci. Technol., A* **2018**, *36*, 061504.
(22) DuMont, J. W.; Marquardt, A. E.; Cano, A. M.; George, S. M. Thermal Atomic Layer Etching of SiO_2 by a "Conversion-Etch" Mechanism Using Sequential Reactions of Trimethylaluminum and Hydrogen Fluoride. *ACS Appl. Mater. Interfaces* **2017**, *9*, 10296−10307.
(23) Zywotko, D. R.; George, S. M. Thermal Atomic Layer Etching of ZnO by a "Conversion-Etch" Mechanism Using Sequential Exposures of Hydrogen Fluoride and Trimethylaluminum. *Chem. Mater.* **2017**, *29*, 1183−1191.
(24) Lemaire, P. C.; Parsons, G. N. Thermal Selective Vapor Etching of TiO_2: Chemical Vapor Etching via WF_6 and Self-Limiting Atomic Layer Etching Using WF_6 and BCl_3. *Chem. Mater.* **2017**, *29*, 6653−6665.
(25) Johnson, N. R.; George, S. M. WO_3 and W Thermal Atomic Layer Etching Using "Conversion-Fluorination" and "Oxidation-Conversion-Fluorination" Mechanisms. *ACS Appl. Mater. Interfaces* **2017**, *9*, 34435−34447.
(26) Xie, W. Y.; Lemaire, P. C.; Parsons, G. N. Thermally Driven Self-Limiting Atomic Layer Etching of Metallic Tungsten Using WF_6 and O_2. *ACS Appl. Mater. Interfaces* **2018**, *10*, 9147−9154.
(27) Johnson, N. R.; Sun, H. X.; Sharma, K.; George, S. M. Thermal Atomic Layer Etching of Crystalline Aluminum Nitride Using Sequential, Self-limiting Hydrogen Fluoride and $Sn(acac)_2$ Reactions and Enhancement by H_2 and Ar Plasmas. *J. Vac. Sci. Technol., A* **2016**, *34*, 050603.
(28) Faraz, T.; Roozeboom, F.; Knoops, H. C. M.; Kessels, W. M. M. Atomic Layer Etching: What Can We Learn from Atomic Layer Deposition? *ECS J. Solid State Sci. Technol.* **2015**, *4*, N5023−N5032.
(29) George, S. M. Atomic Layer Deposition: An Overview. *Chem. Rev.* **2010**, *110*, 111−131.
(30) Clancey, J. W.; George, S. M. In Situ Mass Spectrometer Studies of Volatile Etch Products During Al_2O_3 Atomic Layer Etching Using HF and Trimethylaluminum, *4th International Atomic Layer Etching Workshop, Denver, Colorado, Poster Presentation, July 15−17, 2017, Denver, Colorado*.
(31) Quan, J. L.; Teng, B. T.; Wen, X. D.; Zhao, Y.; Liu, R.; Luo, M. F. Hydrogen Fluoride Adsorption and Reaction on the alpha-Al_2O_3(0001) Surface: A Density Functional Theory Study. *J. Chem. Phys.* **2012**, *136*, 114701.
(32) Wirth, J.; Schacht, J.; Saalfrank, P.; Paulus, B. Fluorination of the Hydroxylated alpha-Al_2O_3 (0001) and Its Implications for Water Adsorption: A Theoretical Study. *J. Phys. Chem. C* **2016**, *120*, 9713−9718.
(33) Kondati Natarajan, S. K.; Elliott, S. D. Modeling the Chemical Mechanism of the Thermal Atomic Layer Etch of Aluminum Oxide: A Density Functional Theory Study of Reactions during HF Exposure. *Chem. Mater.* **2018**, *30*, 5912−5922.
(34) Bendada, A.; Webb, G.; Winfield, J. M. Fluorination of Gamma-Alumina by Sulphur Tetrafluoride, Thionyl Fluoride, Carbonyl Fluoride or Anhydrous Hydrogen Fluoride: A Radiotracer Study. *Eur. J. Solid State Inorg. Chem.* **1996**, *33*, 907−916.
(35) Kemnitz, E.; Menz, D. H. Fluorinated Metal Oxides and Metal Fluorides as Heterogeneous Catalysts. *Prog. Solid State Chem.* **1998**, *26*, 97−153.
(36) Elam, J. W.; Groner, M. D.; George, S. M. Viscous Flow Reactor with Quartz Crystal Microbalance for Thin Film Growth by Atomic Layer Deposition. *Rev. Sci. Instrum.* **2002**, *73*, 2981−2987.
(37) DuMont, J. W.; George, S. M. Pyrolysis of Alucone Molecular Layer Deposition Films Studied Using In Situ Transmission Fourier Transform Infrared Spectroscopy. *J. Phys. Chem. C* **2015**, *119*, 14603−14612.
(38) Hess, D. W.; Deal, B. E. Kinetics of Thermal Oxidation of Silicon in O_2-N_2 Mixtures at 1200 C. *J. Electrochem. Soc.* **1975**, *122*, 579−581.
(39) Kamigaki, Y.; Itoh, Y. Thermal Oxidation of Silicon in Various Oxygen Partial Pressures Diluted by Nitrogen. *J. Appl. Phys.* **1977**, *48*, 2891−2896.
(40) Deal, B. E.; Grove, A. S. General Relationship for Thermal Oxidation of Silicon. *J. Appl. Phys.* **1965**, *36*, 3770−3778.
(41) Böse, O.; Kemnitz, E.; Lippitz, A.; Unger, W. E. S. C 1s and Au 4f(7/2) Referenced XPS Binding Energy Data Obtained with Different Aluminium Oxides, Hydroxides and Fluorides. *Fresenius' J. Anal. Chem.* **1997**, *358*, 175−179.
(42) Roodenko, K.; Halls, M. D.; Gogte, Y.; Seitz, O.; Veyan, J. F.; Chabal, Y. J. Nature of Hydrophilic Aluminum Fluoride and Oxyaluminum Fluoride Surfaces Resulting from XeF_2 Treatment of Al and Al_2O_3. *J. Phys. Chem. C* **2011**, *115*, 21351−21357.
(43) Moulder, J. F.; Stickle, W. F.; Sobol, P. E.; Bomben, K. D. *Handbook of X-ray Photoelectron Spectroscopy*; Perkin-Elmer Corporation, Physical Electronics Division: Eden Praire, MN, 1992.
(44) Mangolini, F.; McClimon, J. B.; Rose, F.; Carpick, R. W. Accounting for Nanometer-Thick Adventitious Carbon Contamination in X-Ray Absorption Spectra of Carbon-Based Materials. *Anal. Chem.* **2014**, *86*, 12258−12265.
(45) Fadley, C. S.; Baird, R. J.; Siekhaus, W.; Novakov, T.; Bergstrom, S. A. Surface Analysis and Angular Distributions in X-ray Photoelectron Spectroscopy. *J. Electron Spectrosc. Relat. Phenom.* **1974**, *4*, 93−137.
(46) McCafferty, E.; Wightman, J. P. An X-ray Photoelectron Spectroscopy Sputter Profile Study of the Native Air-Formed Oxide Film on Titanium. *Appl. Surf. Sci.* **1999**, *143*, 92−100.
(47) Seah, M. P.; Dench, W. A. Quantitative Electron Spectroscopy of Surfaces: A Standard Data Base for Electron Inelastic Mean Free Paths in Solids. *Surf. Interface Anal.* **1979**, *1*, 2−11.
(48) Tanuma, S.; Powell, C. J.; Penn, D. R. Calculations of Electron Inelastic Mean Free Paths for 31 Materials. *Surf. Interface Anal.* **1988**, *11*, 577−589.
(49) Ferguson, J. D.; Weimer, A. W.; George, S. M. Atomic Layer Deposition of Ultrathin and Conformal Al_2O_3 films on BN Particles. *Thin Solid Films* **2000**, *371*, 95−104.
(50) Jost, W. *Diffusion in Solids, Liquids, Gases*; Academic Press Inc. Publishers: New York, 1952.
(51) Massoud, H. Z.; Plummer, J. D.; Irene, E. A. Thermal-Oxidation of Silicon in Dry Oxygen Growth-Rate Enhancement in the Thin Regime 0.1. Experimental Results. *J. Electrochem. Soc.* **1985**, *132*, 2685−2693.

DOI: 10.1021/acs.jpcc.9b00124
J. Phys. Chem. C 2019, 123, 10346−10355